Appl. Phys. B 59, 311–319 (1994)

Applied Physics B Lasers and Optics

VUV spectroscopy of magnetically trapped atomic hydrogen

O. J. Luiten, H. G. C. Werij, M. W. Reynolds, I. D. Setija, T. W. Hijmans, J. T. M. Walraven

Universiteit van Amsterdam, Van der Waals – Zeeman Laboratorium, Valckenierstraat 65/67, NL-1018 XE Amsterdam, The Netherlands (Fax: +31-20/525-5788)

Received 12 November 1993/Accepted 15 May 1994

Abstract. We discuss the experimental and theoretical aspects of absorption spectroscopy of cold atomic hydrogen gas in a magnetostatic trap using a pulsed narrow-band source (bandwidth ≈ 100 MHz) at the Lyman-α wavelength (121.6 nm). A careful analysis of the measured absorption spectra enables us to determine non-destructively the temperature and the density of the trapped gas. The development of this diagnostic technique is important for future attempts to reach Bose-Einstein condensation in trapped atomic hydrogen.

PACS: 67.65.+z, 32.80.Pj, 07.65.−b

The gaseous phase of atomic hydrogen (H) has been studied intensively over the last decade as an important model system for the behavior of dilute neutral gases at ultralow temperatures [1]. Although extremely reactive under ambient conditions, in the spin-polarized state (H↑) and at low temperatures hydrogen is metastable and may be regarded for many practical purposes as an inert gas. As such H is a prime candidate for the observation of Bose-Einstein condensation [1, 2].

To study the properties of ultra-cold gases it is essential to confine the atoms in a surface-free environment. For H↑ this is done with a magnetostatic trap, which may be loaded by a cryogenic technique [3–5]. Recently, we performed the first optical experiments with magnetically trapped H [6, 7]. Using optical absorption spectroscopy as a non-destructive diagnostic tool we can determine gas phase properties like density and temperature. This enables us to study various processes occurring in ultracold gases, such as evaporative cooling and intrinsic decay mechanisms (dipolar relaxation and spin-exchange). Furthermore, we have used our light source to study Doppler cooling and light-induced evaporation of the trapped gas. For our experiments we employ the lowest optical transition for ground state hydrogen, namely the $1^2S \rightarrow 2^2P$ transition (Lyman-α, L_α) at 121.6 nm, which lies in the Vacuum UltraViolet (VUV).

In this paper we focus on the experimental and theoretical aspects of VUV absorption spectroscopy of H↑ in magnetostatic traps [8]. After introducing some nomenclature and the relevant optical transitions, we give a brief description of the trapping field and typical characteristics of the samples. The optical part of the experimental apparatus is described in some detail, addressing VUV generation, VUV optics, frequency stability and frequency tuning. Then we discuss the general phenomenology of light propagation through the sample, and present the detailed theory for the absorption spectrum. We conclude the paper with a discussion of some experimental spectra.

1 Fundamentals

In Fig. 1a we show the hyperfine structure diagram of hydrogen for both the $1^2S_{1/2}$ electronic ground state and the $2^2P_{1/2}$, $2^2P_{3/2}$, and $2^2S_{1/2}$ excited states. By convention the ground state hyperfine levels are labeled a, b, c, and d in order of increasing energy. The b and d states are pure spin states, the a and c states may be expressed as linear combinations of the high field basis states $|m_s, m_i\rangle$, where $m_s = \pm 1/2$ and $m_i = \pm 1/2$ are the electronic and nuclear magnetic quantum numbers, respectively. Aside from the "up" and "down" electron-spin-polarized gases H↑ and H↓ one distinguishes the doubly (electron and proton spin) polarized gases, consisting of b state (H↓↓) or d state (H↑↑) atoms. It is sometimes convenient to label the atoms by the direction of the force caused by magnetic field gradients: high-field seekers ($H_{\downarrow\downarrow}$) and low-field seekers ($H_{\uparrow\uparrow}$). Low-field seekers can be trapped in a B-field minimum. Magnetostatic traps for high-field seekers are not possible because Maxwell's equations do not allow a B-field maximum in free space [9]. Except immediately after loading, magnetostatically trapped gas samples consist mainly of d state atoms because the c state population decays preferentially due to rapid spin-exchange relaxation [10].

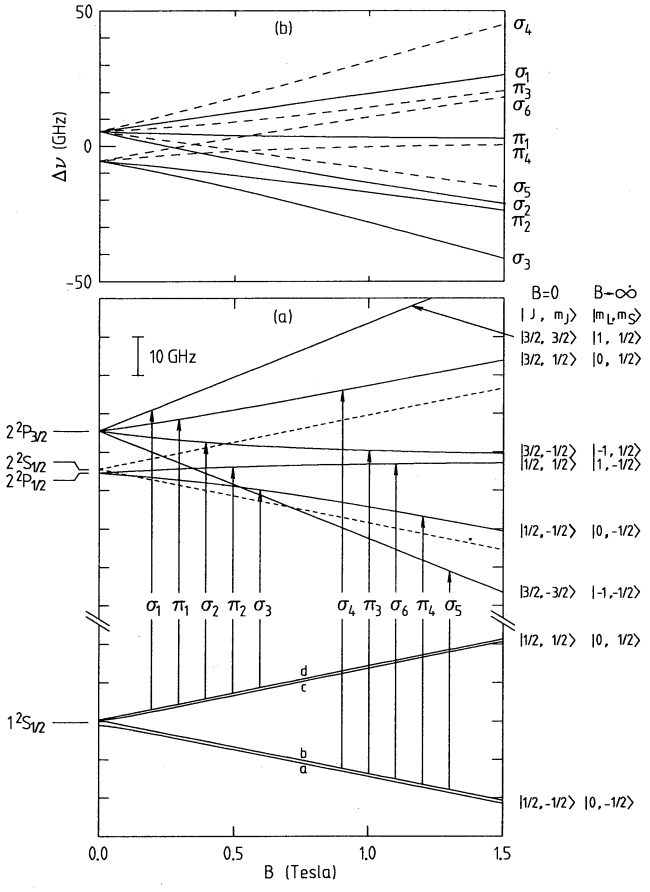

Fig. 1. a Energy levels of the ground state and first excited state of H. The arrows denote the allowed transitions from the doubly polarized ground states. **b** Relative frequencies of the 10 allowed $1S \rightarrow 2P$ fine structure transitions versus magnetic field. *Solid curves:* $H_\uparrow$ transitions; *dashed curves:* $H_\downarrow$ transitions

Also shown in Fig. 1a are the 10 allowed Lyman-α electric dipole transitions from the doubly polarized *b* and *d* states. The most relevant for trapping experiments are the three σ and two π transitions from the *d* state which are labeled σ_1, σ_2, σ_3, π_1, and π_2. The nomenclature refers to the following excited states [11]: $2^2P_{3/2}$, $m_j = 3/2$ (σ_1); $2^2P_{3/2}$, $m_j = 1/2$ (π_1); $2^2P_{3/2}$, $m_j = -1/2$ (σ_2); $2^2P_{1/2}$, $m_j = 1/2$ (π_2); and $2^2P_{1/2}$, $m_j = -1/2$ (σ_3). The corresponding transition frequencies are plotted as a function of *B* in Fig. 1b. The presence of *c* state atoms in the trapped gas gives rise to 10 additional transitions (not shown in Fig. 1), nine of which have the same (fine structure) excited states as the *d* transitions, and one which is strictly forbidden for *d* state atoms and in which the $2^2P_{3/2}$, $m_j = -3/2$ state is excited. Excited state hyperfine effects are negligible for our purpose: First, the hyperfine splitting of the excited states cannot be spectrally resolved since is is much smaller than both the natural linewidth and the bandwidth of our L_α source [11]. Second, the excited states are to a good approximation pure proton-spin states because the excited state hyperfine interaction is much smaller than the Zeeman energy at the typical magnetic field strengths in our experiments ($B \geq 0.05$ T) [12].

The experiments are done with a Ioffe Quadrupole trap, described previously [13]. Four racetrack shaped coils, symmetrically arranged around the *z*-axis, generate a quadrupole field in the *xy*-plane and provide radial confinement. Axial confinement results from (four) dipole coils having the *z*-axis as a common symmetry axis. Together the coils produce a field with a minimum in $|\mathbf{B}|$ on the *z*-axis, which can be approximated near the minimum by [14]

$$\begin{aligned} B_\varrho &= -\alpha\varrho\cos 2\varphi - \beta\varrho z \\ B_\varphi &= \alpha\varrho\sin 2\varphi \\ B_z &= B_0 + \beta z^2 - \beta\varrho^2/2\,, \end{aligned} \tag{1}$$

in cylindrical coordinates ϱ, φ, z, with ϱ the radial distance from the *z*-axis, and φ the azimuthal angle. Typical field parameters are $B_0 = 0.1$ T, $\alpha = 2.2$ T/cm, and $\beta = 0.023$ T/cm^2. For these values the modulus of the magnetic field is well approximated by

$$B = \sqrt{\alpha^2\varrho^2 + (B_0 + \beta z^2)^2}\,. \tag{2}$$

This approximation is adequate, for example, to describe the thermodynamics of the trapped gas. For spectroscopy, however, more precise knowledge of the **B**-field is required and the exact trapping coil geometry is taken into account by introducing *z*-dependent α and β parameters. In the calculation of the spectra we take advantage of the fact that the transverse field $\mathbf{B}_\perp \equiv B_\varrho \mathbf{e}_\varrho + B_\varphi \mathbf{e}_\varphi$ has, to a very good approximation, quadrupolar symmetry.

For a sample of trapped H↑ in internal thermal equilibrium the density distribution is given by

$$n(\mathbf{r}) = n_0 \exp\left[-U_p(\mathbf{r})/k_B T\right], \tag{3}$$

where n_0 is the density of atoms at the field minimum, T the temperature of the trapped gas, and U_p the potential energy of the atoms with respect to the field minimum. For *d* state atoms $U_p(\mathbf{r}) = \mu_B[B(\mathbf{r}) - B_0]$. The sample size depends on temperature. Since on the axis $B_z \rightarrow U_p \propto z^2$, the effective axial length $l_e \propto \sqrt{T}$. For sufficiently low temperature ($T \ll \mu_B B_0/k_B = 67$ mK for $B_0 = 0.1$ T) the trap is approximately harmonic, so the length over width ratio is independent of T. For the typical field parameters mentioned above, $l_e \approx 1$ cm at $T = 10$ mK and the sample is approximately 30 times longer than wide. The sample is probed by a VUV beam (≈ 1 mm beam radius) which propagates through the gas along the *z*-axis. At temperatures immediately after loading ($T \approx 0.1$ K), the radial sample size is comparable to the beam width, at lower temperatures it is smaller. A similar arrangement was used by Helmerson et al. in their experiments with magnetically trapped sodium [15].

2 VUV generation

Our light source is based on pulsed amplification of light from a single-frequency cw ring dye laser, operating at

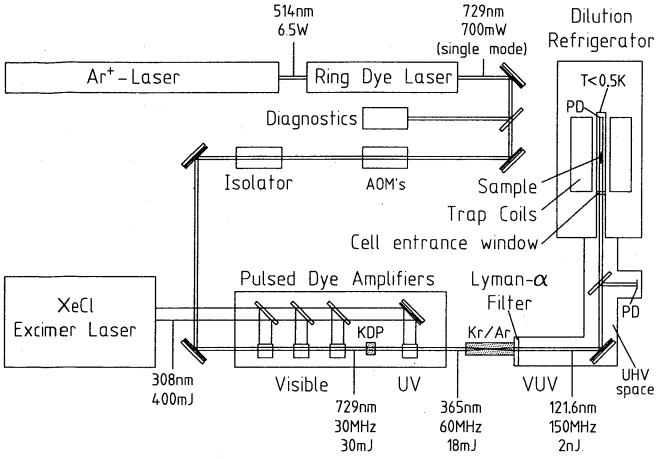

Fig. 2. Schematic diagram of the optical apparatus. Diagnostics stands for the reference cavities and the wavemeter, the Photo-Diodes are denoted by PD

a wavelength of 729.6 nm. The amplified light is frequency-doubled in a KDP crystal and L_α radiation is obtained by third-harmonic generation in a phase-matched mixture of krypton and argon gas [16–19]. A similar, but Nd:YAG based, scheme was used by Cabaret et al. [20] to study Stark shifts in an atomic H beam. Other generating schemes are discussed in the recent literature [21, 22]. The non-resonant tripling scheme was selected for its relative simplicity and reliability.

A schematic diagram of the apparatus is shown in Fig. 2. The ring dye laser (Coherent 699–21) is pumped by an Ar^+ laser (Coherent Innova 200). Cooling the dye (pyridine 2 in ethylene glycol) to 9° C, the single-mode output of the dye laser (effective linewidth 1.5 MHz) amounts to $\approx$750 mW at 6.5 W pump power. After passing through an optical isolator the main part of the cw light is sent through a three-stage rhodamine 700 pulsed dye amplifier (Lambda Physik 2003) to enable efficient frequency-doubling. The dye amplifiers are pumped by a XeCl-excimer laser (Lambda Physik LPX 210 i, 308 nm), selected for its long pulses (20 ns) which ensure the smallest possible bandwidth. It has the additional advantage of providing a high pulse rate (up to 100 Hz). The ensuing ultraviolet (UV, 364.8 nm) is amplified once more in a DMQ/propylene carbonate dye cuvette. At a repetition rate of 50 Hz the energy of the amplified UV light is typically $\approx$18 mJ/pulse. Its bandwidth was determined using a confocal etalon of 150 MHz Free Spectral Range (FSR) and was found to be 40–60 MHz, a factor 2–3 larger than that of a Fourier-limited Gaussian pulse of equivalent duration (20 ns). From this we obtain an estimate for the upper bound to the bandwidth at L_α of 180 MHz.

For tripling, the UV light beam (typical beam radius 2 mm) is focused by an $f = 15$ cm lens into a gas mixture of, typically, 160 mbar Kr and 480 mbar Ar (Fig. 3). The power generated at L_α corresponds to $2 \times 10^9 L_\alpha$ photons per pulse. The conversion efficiency is $\approx 10^{-7}$. The maximum power level is limited by the occurrence of dielectric breakdown in the Kr/Ar mixture. We have observed that the UV beam profile shows an increasingly severe higher-order mode structure for aging amplifier dyes, negatively affecting the conversion efficiency [23] and the threshold for dielectric breakdown.

3 VUV optics

The L_α and the 10^7 times stronger copropagating UV light are separated in a monochromator, using the refraction and dispersion of two MgF_2 lenses (Fig. 3). The first lens (L_1), which is placed off-axis with respect to the incoming beam, focuses the L_α beam onto a 0.5 mm diameter aperture, while the fundamental beam is collimated and deflected via a mirror onto a beam dump. A second MgF_2 lens (L_2), which collimates the L_α beam, is also used off-axis to provide additional spectral filtering. This double filter arrangement reduces the intensity of the 365 nm radiation by more than 9 orders of magnitude. Lens L_2 is mounted in an *xyz* translation stage to facilitate collimation and alignment. A drawback of the off-axis use of the lenses is that it introduces astigmatism. Nevertheless, by adjusting the horizontal position of L_2, we were able to obtain a nearly circular beam cross section with a diameter of about 2 mm at the center of the cryogenic magnetic trap, located 1.2 m from the tripling cell. The L_α beam is guided into the cryostat from below, via a 45° high quality (reflectivity $\approx$85%) VUV mirror (Acton Research Corporation).

The volume between L_1 and L_2 is constantly flushed with pure Ar at a pressure of about 20 Torr to avoid deterioration of the optics due to sputtering of impurities by the UV beam. The vacuum section behind L_2 is separated from the trapping volume by a 1 mm thick, indium sealed, MgF_2 cell entrance window, at sub-Kelvin temperatures. We exclusively use all-metal seals, thus eliminating diffusive leaks due to the permeability

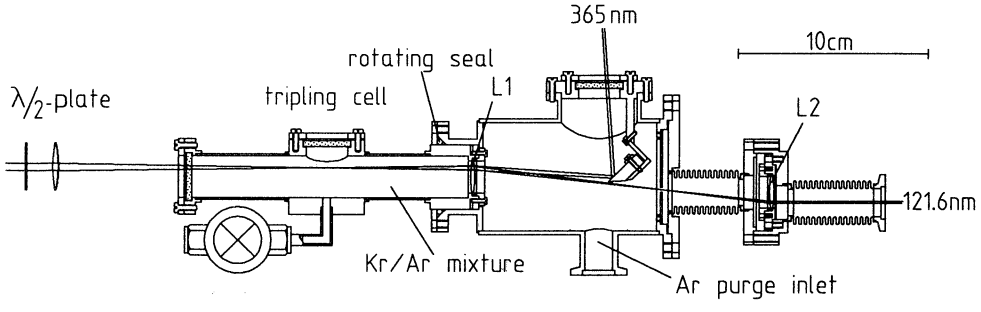

Fig. 3. The tripling cell and monochromator

of rubber O-rings. Furthermore, we close a valve separating the cryostat from the room-temperature vacuum section, when not taking data. These precautions allow us to operate the system during a period of several months without a noticeable build-up of cryo-deposits on the cell window.

A MgF_2 beam splitter between the mirror and the cryostat couples 5–10% of the beam onto a solar blind vacuum diode (Hamamatsu R1187). This offers the possibility to perform ratio measurements, largely eliminating the noise due to the $\approx 10\%$ pulse-to-pulse fluctuations of the L_α intensity. About 2% (5×10^7 photons/pulse) of the generated VUV reaches the H sample.

The optical transmission of the trapped H↑ gas is measured with a GaAsP Schottky photodiode (Hamamatsu G1126, sensitive area 2.3 mm × 2.3 mm) mounted at the end of the cell. An important property of this type of diode is that it has good long-term reproducibility under VUV irradiation [24]. With the protective window removed, the diode is found to have a quantum efficiency of 14% at L_α for temperatures down to liquid nitrogen. At liquid helium temperature and below the quantum efficiency is about 10% at the specified maximum bias voltage of 5 V. The characteristics of the detector are not affected by magnetic fields up to 1.5 T. The main advantage of the diode over of a (solar blind) metal photocathode is that the diode is sensitive to both UV and HeNe laser light. This allows us to verify the absence of 365 nm background and facilitates the rather delicate alignment of the optics.

Although the generated VUV is linearly polarized [25, 26], we found that its polarization inside the H cell is in general elliptical. We attribute the change in polarization to the dielectrically coated aluminum 45° VUV mirror. By adjusting the plane of polarization of the incoming UV light using a half-wave plate, we can continuously change the VUV polarization in the H cell from left-circular via linear to right-circular.

4 Frequency stability

To determine the frequency of the L_α radiation to within one natural linewidth ($\Gamma/2\pi = 100$ MHz), the cw dye laser frequency should be known to within ≈ 16 MHz. For this purpose we use a piezo-driven confocal Fabry-Perot etalon, scanning ≈ 6 GHz at a repetition rate of 10 Hz. The FSR of the etalon is 3.0 GHz and its measured finesse is 175. To remove errors arising from the inherent drift of the piezo material, we use a second etalon, without piezo material, which has the same FSR and resolution. This fixed etalon serves as a reference for calibration of the piezo-driven etalon. Any ambiguity with regard to the order of operation of the etalons is eliminated with a commercial wavemeter (Burleigh WA-20) having a resolution (0.3 GHz) better than the FSR of the etalons.

Stable operation was obtained by constructing the body of the etalons from invar metal with a thermal expansion coefficient of $\approx 10^{-6}\,K^{-1}$. The choice of the piezo material (Quartz & Silice, P7-62) was motivated by its small thermal expansion coefficient ($\approx 2 \times 10^{-6}\,K^{-1}$) and low power dissipation. Using a tubular piezo of length 9 mm and wall thickness 1 mm the etalon scans ≈ 18 MHz/V. The linearity of the piezo has been measured using the transmission peaks of a 150 MHz FSR etalon as frequency markers. Over a scanning range of 6 GHz the deviation from linearity was within the accuracy of the measurement (≈ 5 MHz).

The thermal expansion coefficients mentioned above imply a frequency shift of ≈ 1 MHz/mK for both etalons. Therefore, the etalons are mounted in a hermetically sealed precision thermostat, developed for critical point experiments by Michels and Van Lieshout in our laboratory [27]. The short-term stability of this thermostat is better than 20 μK/h. To determine the long-term stability of the thermostat-etalon combination we monitored the drift of the etalon transmission peaks with respect to the $4^2S_{1/2} \rightarrow 6^2S_{1/2}$ Doppler-free two-photon transition in potassium [28], which has a wavelength of 728.6 nm and is observed through the $6^2S_{1/2} \rightarrow 4^2P_{1/2,3/2}$ cascade fluorescence. Over a period of 10 days the tunable etalon showed a constant drift of 365 kHz/h, while the fixed etalon remained stable within 5 MHz.

5 Frequency tuning

The frequency of the L_α radiation can be varied by tuning the cw dye laser frequency, which is locked to a transmission peak of the tunable etalon. This is perfectly suitable for relatively slow scans. In some cases, however, the possibility of pulse-to-pulse frequency switching is desirable to monitor the spectrum at specific discrete points during transient conditions when the spectrum

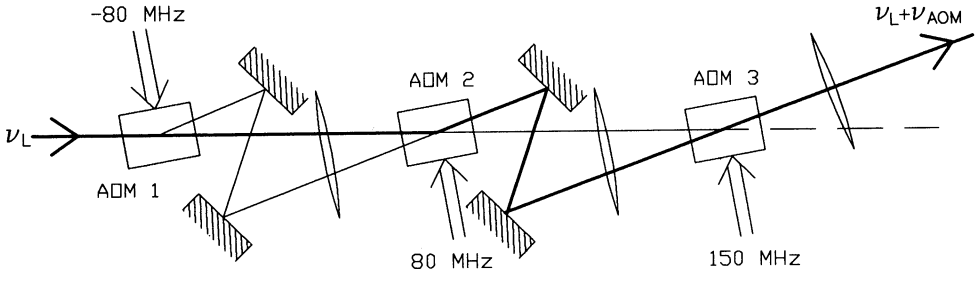

Fig. 4. Layout of the AOM arrangement. For clarity, the *angles* have been exaggerated. The *thick line* denotes the light path when AOM 2 (+80 MHz) is switched on

changes rapidly. The latter method was used to infer the temperature and density of the trapped H↑ gas with a time resolution of 0.5 s during evaporative cooling [6]. Furthermore, during optical cooling it allows for occasional excursions to different parts of the spectrum, e.g., for thermometry, while the sample is irradiated at the optimal cooling frequency most of the time [7]. To enable the pulse-to-pulse switching, the cw dye laser light is guided through an arrangement of three Acousto-Optic Modulators (AOMs), which is depicted schematically in Fig. 4. The alignment of the mirrors is such that, if any one of the three AOMs is switched on, the first-order diffracted beam enters the amplifier section along the same path, with no admixture of the zeroth-order undeflected light. With this AOM chain, the frequency of the cw beam is shifted either -80 MHz, $+80$ MHz or $+150$ MHz with respect to the incoming frequency. For the L_α light this corresponds to two incremental steps of 0.96 GHz and 0.42 GHz, respectively. The requirement for the alignment of the diffracted beams is rather stringent, since the distances from the AOM chain to the pulsed dye amplifiers and to the H↑ sample in the cryostat are 7 m and 15 m, respectively. To avoid drifting of the beam alignment due to rf heating, the AOMs are driven only during a 0.3 ms period, synchronized with the firing of the excimer laser.

We have repeatedly checked whether the polarization of the generated L_α light was dependent on the particular AOM used. When scanning across the H spectrum, while simultaneously switching rapidly between the three AOMs, we always find that, apart from the desired frequency shift, all three spectra are identical.

6 Absorption spectroscopy

Before going into the details of calculating the absorption spectra and comparison with experiment, we make some general remarks on the light propagation through the trapped gas.

In our experiments the L_α enters the experimental cell along the z-axis (Fig. 2) and passes through the gas, being partially scattered before hitting the photodiode. The resonant absorption cross section for L_α can be as high as $3\lambda_\alpha^2/2\pi$, which at a typical density $n=10^{12}\,\mathrm{cm}^{-3}$ corresponds to a resonant extinction length $2\pi/(3n\lambda_\alpha^2)=0.14$ mm. In practice the resonant absorption cross section is smaller due to Doppler broadening and polarization effects, but still sufficiently large to make the sample optically thick at moderate densities. Under these conditions the sample actually casts a shadow on the photodiode. Since the dimensions of the photodiode are comparable to the beam diameter and comparable to or larger than the radial sample size, the intensity of the light incident on the photodiode is generally strongly varying over its surface.

The combination of the spin-polarization of the atoms and strong light absorption induces substantial changes in the polarization of the light while it propagates through the sample. To illustrate this, suppose that linearly polarized light is incident on the sample at a frequency which is resonant on the axis with a σ^- transition, but, due to Zeeman splitting, not in resonance with any σ^+ transition. On the axis the magnetic field vector is parallel to the direction of the propagating light so only right-circularly polarized light will be absorbed, changing the polarization of the light from linear to left-circular. Off-axis, in somewhat higher field, the same light beam may drive a π transition since off-axis the magnetic field vector also has a component perpendicular to the direction of the light propagation. In this case the polarization remains linear.

Furthermore, optical thickness goes hand in hand with strong dispersive effects. To illustrate this we neglect the vector character of the light for the moment. For a dilute medium of motionless two-level atoms the refractive index η at a frequency ω close to the resonant frequency ω_0 is then given by

$$\eta-1=\frac{\pi n\gamma(\omega_0-\omega)}{k^3[(\omega_0-\omega)^2+\gamma^2]}, \tag{4}$$

with $k=\omega/c$ and $\gamma\equiv\Gamma/2$. For typical densities $n\lesssim 10^{14}\,\mathrm{cm}^{-3}$, $|\eta-1|\lesssim 10^{-3}$. Hence the gas is a very dilute dielectric medium and refraction is completely negligible. Dispersion, however, is very important. A light wave travelling a distance Δz through the sample acquires a phase shift $\Delta\varphi=(\eta-1)k\Delta z$ with respect to a wave of the same frequency in vacuum. If the frequency of the light is tuned near resonance, $\omega_0-\omega=\gamma$, a phase shift $\Delta\varphi=1$ is acquired over a distance $\Delta z=8\pi/n\lambda_\alpha^2$, which is twice the extinction length at this detuning. Such effects strongly enhance the polarization changes caused by absorption of the light, discussed above. This holds even for large detuning when the absorption is small. For example, tuned halfway between a σ^+ and a σ^- line both circular components of a linearly polarized light beam will be weakly, but equally, absorbed, thus keeping the light linearly polarized. The real parts of the susceptibilities associated with the two transitions, however, have opposite signs, causing an increasing phase shift between the two circular wave components which implies (Faraday) rotation of the total, linear, polarization.

The evolution of polarization during propagation through the sample can strongly influence subsequent absorption. Therefore, in order to calculate absorption spectra reliably, it is necessary to keep track of the intensity, polarization, and phase of the light propagating through the sample. Furthermore, the magnetic field strength B_0 at the center of the trap is not sufficiently high to spectrally separate the allowed transitions completely. Therefore, when propagating light through a sample, the contributions of all allowed transitions to the extinction and, in particular, the dispersion of the light have to be taken into account simultaneously. In addition, at temperatures $k_BT\gtrsim\mu_BB_0$ ($T\gtrsim 67$ mK for $B_0=0.1$ T) there is a strong overlap between absorption lines due to the fact that light of a certain frequency can come into resonance with different transitions at different positions in the sample.

7 Theory

First, we review some aspects of the extinction of a weak cw light beam in a dilute gas of resonant scatterers, to the extent necessary for the description of the experimental spectra [29]. The treatment is semiclassical, with a classical representation of the electromagnetic field but a quantum description of the atoms.

We are interested in the extinction of a plane electromagnetic wave of wave vector $\mathbf{k}$ and frequency ω propagating in the z direction through a dilute polarizable medium, so we write the electric field vector $\mathbf{E}$ and the induced polarization $\mathbf{P}$ in the form

$$\begin{aligned}\mathbf{E}(\mathbf{r}, t) &= \mathbf{E}_0(\mathbf{r})e^{i(kz-\omega t)},\\ \mathbf{P}(\mathbf{r}, t) &= \mathbf{P}_0(\mathbf{r})e^{i(kz-\omega t)},\end{aligned} \tag{5}$$

where $k=|\mathbf{k}|=\omega/c=\omega\sqrt{\varepsilon_0\mu_0}$. Using the slowly varying amplitude approximation, Maxwell's equations for a dielectric medium can be reduced to

$$\frac{\partial \mathbf{E}_0}{\partial z} = \frac{ik}{2\varepsilon_0}[\mathbf{P}_0-(\mathbf{P}_0\cdot\mathbf{e}_z)\mathbf{e}_z], \tag{6}$$

where $\mathbf{e}_z$ is the unit vector in the z-direction. This is our basic equation for the calculation of the propagation of a L_α beam through a sample of trapped H↑. The induced polarization gives rise to both extinction and dispersion of the light. $\mathbf{P}_0$ is in general not parallel to $\mathbf{E}_0$, but depends on the local orientation of the $\mathbf{B}$-field. The induced polarization can be written as

$$\mathbf{P}_0=\varepsilon_0\overleftrightarrow{\chi}\mathbf{E}_0, \tag{7}$$

where $\overleftrightarrow{\chi}$ is the complex susceptibility tensor.

Consider first a medium of motionless atoms. The induced polarization due to electric dipole transitions between ground state $|h\rangle$ and excited state $|j\rangle$ is equal to the product of the density n_h of atoms in ground state $|h\rangle$ and the expectation value of the electric transition dipole moment. For light intensities far below saturation of the transitions one may derive that

$$\mathbf{P}_0 = \sum_{h,j} n_h \frac{(\mathbf{d}_{jh}\cdot\mathbf{E}_0)\mathbf{d}_{hj}}{\hbar(\omega_{hj}-\omega-i\gamma)}, \tag{8}$$

with ω_{hj} the transition frequencies, $\mathbf{d}_{hj}\equiv\langle h|\mathbf{d}|j\rangle$ the electric dipole transition matrix elements, and $\gamma=\gamma_j\equiv k^3\sum_f|\mathbf{d}_{fj}|^2/(6\pi\varepsilon_0\hbar)$. The latter equality only holds if the splitting of the ground state sublevels h and of the excited state sublevels j is negligible with respect to ω_{hj}, as is clearly the case for the $1S\rightarrow 2P$ transitions in H. From (8) follows immediately the susceptibility tensor $\overleftrightarrow{\chi}_0$ for a gas at $T=0$:

$$\overleftrightarrow{\chi}_0 = \frac{6\pi}{k^3}\sum_{h,j} n_h \frac{\mathbf{d}_{hj}\mathbf{d}_{hj}^*\gamma}{\sum_f|\mathbf{d}_{fj}|^2(\omega_{hj}-\omega-i\gamma)}. \tag{9}$$

For atoms in motion the transitions are Doppler broadened and, assuming a Maxwell-Boltzmann velocity distribution, the susceptibility is

$$\overleftrightarrow{\chi} = i\frac{6\pi^{3/2}}{k^3}\sum_{h,j} n_h \frac{\mathbf{d}_{hj}\mathbf{d}_{hj}^*}{\sum_f|\mathbf{d}_{fj}|^2}\frac{\gamma}{b}w(\zeta_{hj}), \tag{10}$$

where $b=k\sqrt{2k_BT/m}$, $w(\zeta)=e^{-\zeta^2}\operatorname{erfc}(-i\zeta)$, and $\zeta_{hj}=(\omega-\omega_{hj}+i\gamma)/b$. The real part of the complex error function w is the Voigt profile describing a Doppler broadened Lorentzian line. For $b\gg\gamma$, i.e., for $T\gg 2.2$ mK for H, the Voigt lineshape function approaches a Gaussian function with a FWHM Doppler linewidth $\Delta\omega_D\equiv 2\pi\Delta\nu_D=2b\sqrt{\ln 2}$. In our case $\Delta\nu_D/\sqrt{T}=1.76\,\mathrm{GHzK}^{-1/2}$. For $b\ll\gamma$, (10) reduces to (9).

Now we specialize to our experimental situation, namely the propagation of light parallel to the symmetry axis of a Ioffe quadrupole trap. To this purpose we introduce the vector basis $(\mathbf{e}_1, \mathbf{e}_2, \mathbf{e}_3)$, with $\mathbf{e}_3$ parallel to $\mathbf{k}$, $\mathbf{e}_1$ given by the direction of the magnetic field component $\mathbf{B}_\perp$ perpendicular to $\mathbf{k}$, and $\mathbf{e}_2$ perpendicular to both $\mathbf{e}_1$ and $\mathbf{e}_3$:

$$\begin{aligned}\mathbf{e}_1 &= \mathbf{B}_\perp/B_\perp,\\ \mathbf{e}_2 &= (\mathbf{k}\times\mathbf{B})/kB,\\ \mathbf{e}_3 &= \mathbf{k}/k.\end{aligned} \tag{11}$$

Since the *direction* of the transverse magnetic field component $\mathbf{B}_\perp$ is independent of z, the basis (11) is invariant during propagation of the light through the sample.

The electric field amplitude $\mathbf{E}_0$ may be expressed in either a linear or a circular polarization basis:

$$\mathbf{E}_0 = E_{01}\mathbf{e}_1+E_{02}\mathbf{e}_2 = E_{0+}\mathbf{e}_+ + E_{0-}\mathbf{e}_-, \tag{12}$$

where $\mathbf{e}_\pm\equiv(\mathbf{e}_1\pm i\mathbf{e}_2)/\sqrt{2}$. The unit vector $\mathbf{e}_+$ ($\mathbf{e}_-$) corresponds to left (right)-circularly polarized light. As we shall see, the circular polarization basis is the most convenient.

We also introduce the auxiliary basis $(\mathbf{e}'_1, \mathbf{e}'_2, \mathbf{e}'_3)$, which is obtained by rotating basis (11) about $\mathbf{e}_2$ so that $\mathbf{e}'_3=\mathbf{B}/B$. This is useful because $\mathbf{B}$ is the quantization axis for $\overleftrightarrow{\chi}$. The matrix representation of $\overleftrightarrow{\chi}$ with respect to the $(\mathbf{e}'_\pm, \mathbf{e}'_3)$ basis has a simple diagonal form:

$$[\overleftrightarrow{\chi}]' = \begin{pmatrix}\chi_+ & 0 & 0\\ 0 & \chi_- & 0\\ 0 & 0 & \chi_z\end{pmatrix}. \tag{13}$$

Here χ_+ is defined by

$$\chi_+ \equiv i\frac{6\pi^{3/2}}{k^3}\sum_{h,j} n_h \frac{\gamma_{hj}}{b}w(\zeta_{hj}), \tag{14}$$

where the branching ratios

$$\frac{\gamma_{hj}}{\gamma} = \frac{|\mathbf{d}_{hj}|^2}{\sum_f|\mathbf{d}_{fj}|^2}, \tag{15}$$

and the h, j summation is restricted to σ^+ transitions. χ_- and χ_z are defined analogously, with the h, j summation restricted to, respectively, σ^- and π transitions. The B-dependence of the branching ratios γ_{hj}/γ and of the resonant transition frequencies ω_{hj} of atomic hydrogen can be found, for instance, in [30].

The unitary matrix U for transformation from a $(\mathbf{e}_\pm, \mathbf{e}_3)$ representation to a $(\mathbf{e}'_\pm, \mathbf{e}'_3)$ representation is given by

$$U = \frac{1}{2}\begin{pmatrix} \cos\theta+1 & \cos\theta-1 & -\sqrt{2}\sin\theta \\ \cos\theta-1 & \cos\theta+1 & -\sqrt{2}\sin\theta \\ \sqrt{2}\sin\theta & \sqrt{2}\sin\theta & 2\cos\theta \end{pmatrix}, \tag{16}$$

where θ is the angle between $\mathbf{B}$ and $\mathbf{k}$ ($\cos\theta = B_z/B$, $\sin\theta = B_\perp/B$). The matrix representation of $\overleftrightarrow{\chi}$ in the $(\mathbf{e}_\pm, \mathbf{e}_3)$ basis is

$$[\overleftrightarrow{\chi}] = U^{-1}[\overleftrightarrow{\chi}]' U. \tag{17}$$

We thus find that the propagation of the electric field amplitude $\mathbf{E}_0$ (6, 7) is described by the following set of coupled differential equations:

$$\begin{aligned} \partial E_{0+}/\partial z &= (ik/8)\{[\chi_+(1+\cos\theta)^2+\chi_-(1-\cos\theta)^2 \\ &\quad +2\chi_z\sin^2\theta]E_{0+}+(2\chi_z-\chi_+-\chi_-)\sin^2\theta E_{0-}\}, \\ \partial E_{0-}/\partial z &= (ik/8)\{(2\chi_z-\chi_+-\chi_-)\sin^2\theta E_{0+}+[\chi_+(1-\cos\theta)^2 \\ &\quad +\chi_-(1+\cos\theta)^2+2\chi_z\sin^2\theta]E_{0-}\}. \end{aligned} \tag{18}$$

For $\theta=0$ the equations are decoupled and χ_z drops out of the equations, or, in other words, the π transitions do not influence the propagation of the light:

$$\partial E_{0\pm}/\partial z = (ik/2)\chi_\pm E_{0\pm}. \tag{19}$$

In our system this is the case along the symmetry axis of the trap. For $\theta=\pi/2$ the equations also reduce to a simple decoupled form when written in the linear polarization basis:

$$\begin{aligned} \partial E_{01}/\partial z &= (ik/2)\chi_z E_{01}, \\ \partial E_{02}/\partial z &= (ik/4)(\chi_+ + \chi_-)E_{02}. \end{aligned} \tag{20}$$

In our Ioffe trap θ varies and the full coupled equations must be integrated for every point in the xy-plane that falls within the sensitive area of the photodiode. However, for a light beam with an axially symmetric intensity distribution and uniform but arbitrary polarization, the dependence on the azimuthal angle φ can be eliminated by making use of the quadrupolar symmetry of the trapping field. Suppose that for $\varphi=0$ and a given distance from the symmetry axis the initial electric field amplitude is given by $\mathbf{E}_0 = E_{0+}\mathbf{e}_+ + E_{0-}\mathbf{e}_-$. The E_{0+} component gives rise to a field amplitude $E_{+\,+}\mathbf{e}_+ + E_{+\,-}\mathbf{e}_-$ on the photodiode surface and the E_{0-} component to a field amplitude $E_{-\,+}\mathbf{e}_+ + E_{-\,-}\mathbf{e}_-$. Using the quadrupolar symmetry of the field and the definition (11) it is straightforward to derive that the intensity I_d on the detector surface for an arbitrary angle φ can be written as

$$\begin{aligned} I_d = \frac{1}{2}\varepsilon_0 c[&|E_{+\,+}|^2+|E_{+\,-}|^2+|E_{-\,+}|^2+|E_{-\,-}|^2 \\ &+\mathrm{Re}\,(E_{+\,+}E^*_{-\,+}+E_{-\,-}E^*_{+\,-})\cos 2\varphi]. \end{aligned} \tag{21}$$

Thus, the intensity distribution on the detector surface can be completely determined by integrating (18) for a single value of φ. In addition, since the photodiode is square, the φ-dependent term in (21) averages to zero in the measurement. The observed signal is proportional to the sum of the average intensities associated with the separate circular polarization components, independent of their relative phase. Therefore, the absorption spectrum for input light of arbitrary polarization is a simple linear combination of the spectra for left and right-circularly polarized light.

To compare with experiment we convolve the theoretical spectra with a 100 MHz FWHM Lorentzian to account for the instrumental bandwidth of our L_α source.

8 Experimental spectra

We will now present several examples of experimental spectra and discuss their interpretation, which allows us to determine the density and the temperature of the trapped gas.

In Fig. 5 two spectra are shown for the same sample, at a relatively high temperature, one taken with right and one with left-circularly polarized light. The **B**-field geometry used is characterized by the field parameters given below (1). The scan time for each spectrum was 30 s, which is approximately the maximum allowable time at gas densities $\approx 10^{12}$ cm^{-3} for taking spectra with the aim of determining the temperature and the density of the trapped gas. Longer scan times lead to non-negligible particle loss during the scan, either through intrinsic loss mechanisms or through optical pumping to H$\downarrow$ states. A scan time of 30 s, however, gives a satisfactory signal-to-noise ratio.

The spectra consist of five partially overlapping lines, which can be identified with the H$\uparrow$ transitions σ_1, σ_2, σ_3, π_1, and π_2 (Fig. 1b). Since $\mathbf{k}\cdot\mathbf{B} > 0$ in our setup, right-

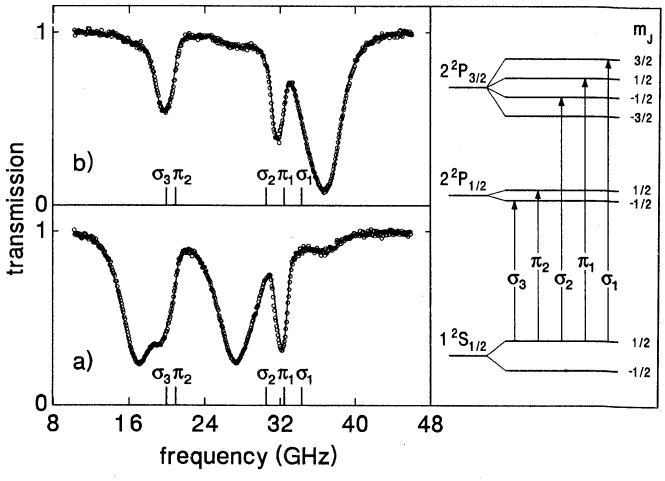

Fig. 5a, b. Absorption spectra, recorded with (**a**) right- and (**b**) left-circularly polarized light, and energy level diagram defining the five allowed transitions. The *solid lines* are calculated spectra for $T = 51 \pm 12$ mK and (**a**) $n_0 = (4.4 \pm 1.0) \times 10^{12}$ cm^{-3} and (**b**) $n_0 = (3.3 \pm 0.8) \times 10^{12}$ cm^{-3}. The frequency is relative to (3/4) $R_\infty(1+m_e/m_p)^{-1}$, where R_∞ is the Rydberg constant and m_e/m_p the electron-proton mass ratio. The vertical bars denote the resonant frequencies of the five allowed transitions for $B = B_0$

circularly polarized light mainly excites the σ^- transitions σ_2 and σ_3 (Fig. 5a), and left-circularly polarized light the σ^+ transition σ_1 (Fig. 5b). The π transitions respond to linearly polarized light and are therefore equally excited by both helicities. The asymmetric shapes of the lines are due to Zeeman shifts of the resonant frequencies and reflect the distribution of particles in the trapping field. The blue wing of the σ_1 line, for instance, is due to absorption by atoms in relatively high fields, consistent with the positive sign of the Zeeman shift. On the other hand, the σ_2, σ_3, and π_2 transitions have negative Zeeman shifts and are consequently broadened to the red. The π_1 line displays no appreciable asymmetric broadening, due to its small Zeeman shift. In the spectra under consideration Doppler broadening and the natural linewidth are less important.

The temperature and density of the trapped gas are found by comparing calculated and experimental spectra. In the fitting procedure there are three free parameters: the central density n_0, the fraction of atoms in the c state, and the temperature of the trapped gas T. The hyperfine structure of the spectra, due to c state atoms, becomes resolvable only at $T \lesssim 10$ mK and is not important for the spectra under consideration. With the remaining two parameters it is possible to obtain very good fits, as is shown in Fig. 5. We find for both spectra a temperature $T = 51 \pm 12$ mK, while for the first spectrum (a) $n_0 = (4.4 \pm 1.0) \times 10^{12}$ cm^{-3}, and for the second spectrum (b) $n_0 = (3.3 \pm 0.8) \times 10^{12}$ cm^{-3}. Uncertainties of $\approx 25\%$ are typical for our experiments and result primarily from imprecise knowledge of the beam profile.

The spectra shown in Fig. 5 exhibit several interesting features. Striking is the fact that, although $\mathbf{k} \cdot \mathbf{B} > 0$, there is clearly a contribution of the σ^+ transition σ_1 present in the spectrum of Fig. 5a and some traces of absorption on the σ^- transitions σ_2 and σ_3 in the spectrum of Fig. 5b. This is not due to incomplete polarization of the light, but to the finite angle θ between $\mathbf{k}$ and $\mathbf{B}$ (off-axis). It is immediately clear from (18) that if $\theta \neq 0$ the component E_{0-} is also absorbed on σ^+ transitions and the component E_{0+} on σ^- transitions, because the projection of the oscillating electric field vector of a purely circularly polarized light beam on a plane $\perp \mathbf{B}$ is elliptical and thus also contains a circular component with opposite helicity.

A second point of interest is the fact that the absorption is enhanced by optical activity. Circularly polarized light can be written as the sum of two perpendicular, phase-shifted linearly-polarized components of equal amplitude. Since π resonances only affect the linearly polarized component parallel to the transverse magnetic field component $\mathbf{B}_\perp$, one would expect that π-absorption of circularly polarized light cannot exceed 50%. In the spectra of Fig. 5, however, we observe that the maximum absorption on the π lines is substantially higher. The extra absorption is too strong to be attributed to the wings of σ lines. To explain the origin of this feature, (18) is rewritten in the linear polarization basis, defined by the local orientation of the magnetic field (11, 12):

$$\begin{aligned} \partial E_{01}/\partial z &= (ik/4)\{[(\chi_+ + \chi_-)\cos^2\theta + 2\chi_z \sin^2\theta]E_{01} \\ &\quad - i(\chi_+ - \chi_-)E_{02}\}\cos\theta, \\ \partial E_{02}/\partial z &= (ik/4)[(\chi_+ + \chi_-)E_{02} + i(\chi_+ - \chi_-)E_{01}\cos\theta]. \end{aligned} \tag{22}$$

Recall that $\mathbf{e}_1$ is by definition parallel to $\mathbf{B}_\perp$, so only the component E_{01} is directly absorbed on π transitions. However, the equations are coupled so the component E_{02} is also affected – indirectly – by π transitions. Suppose, for instance, that π-absorption has reduced E_{01} to zero. If the frequency is tuned between a σ^+ and a σ^- resonance in such a way that linearly polarized light is equally absorbed on both transitions, i.e., $\mathrm{Im}\,\chi_+ = \mathrm{Im}\,\chi_-$ and thus $\mathrm{Re}\,\chi_+ = -\mathrm{Re}\,\chi_-$, then (22) are coupled by a real coefficient $(k/4)(\chi_+ - \chi_-)\cos\theta$. Consequently, the amplitude E_{01} will grow, in phase with the existing component E_{02}, which means that the total polarization vector $\mathbf{E}_0 = E_{01}\mathbf{e}_1 + E_{02}\mathbf{e}_2$ remains linear but starts rotating in the $(\mathbf{e}_1, \mathbf{e}_2)$-plane ($= xy$-plane). In this way the polarization, initially perpendicular to $\mathbf{B}_\perp$, will acquire a linear component parallel to $\mathbf{B}_\perp$ and will be absorbed subsequently on π transitions. In other words, due to Faraday rotation both initial linear polarization components E_{01} and E_{02} are absorbed on π transitions so the absorption can be higher than 50%. At high densities we observed as much as 90% absorption on π lines. There is only pure Faraday rotation if $\mathrm{Im}\,\chi_+ = \mathrm{Im}\,\chi_-$. At other frequencies the polarization will in general be elliptical, with the eccentricity and the orientation of the principal axes of the ellipse continuously changing as a function of z.

Close inspection of the spectra shown in Fig. 5 reveals another subtle feature, namely, the frequency for maximum absorption of the π_1 line is different for left- and right-circularly polarized light. The π_1 line seems to be repelled by σ lines: for left-circularly polarized light the σ_1 line is strongest and the π_1 line is shifted to the red, while for right-circularly polarized light the σ_2 line is strongest and the π_1 line is shifted to the blue. However, in both cases the π_1 line is on the slope of a strong σ line and one would expect shifts in opposite directions. This phenomenon can be traced back to the imaginary part of the coupling coefficient $(k/4)(\chi_+ - \chi_-)\cos\theta$ in (22). Suppose at $z = 0$ we have left-circularly polarized light $\mathbf{E}_0 = E_{01}(\mathbf{e}_1 + i\mathbf{e}_2)$. The coupling term in (22) will cause E_{01} to change at a rate

$$(ik/4)(\chi_+ - \chi_-)\cos\theta E_{01}. \tag{23}$$

At frequencies where σ^--absorption is stronger, i.e., $\mathrm{Im}\,(\chi_+ - \chi_-) < 0$, E_{01} increases, leading to increased dissipation on the π transition. Hence π-absorption of left-circularly polarized light is enhanced if $\mathrm{Im}\,(\chi_+ - \chi_-) < 0$, which means the peak of the π_1 line will be shifted towards the σ_2 line, as is observed. Analogously, π-absorption of right-circularly polarized light is enhanced if $\mathrm{Im}\,(\chi_+ - \chi_-) > 0$ an the π_1 line will be shifted towards the σ_1 line.

In Fig. 6 a spectrum is shown of a sample at a relatively low temperature, which was taken with right-circularly polarized light. The low temperature was obtained by light-induced evaporation [7]. The scan time was 10 s and only the $2^2P_{3/2}$ multiplet was recorded. The **B**-field

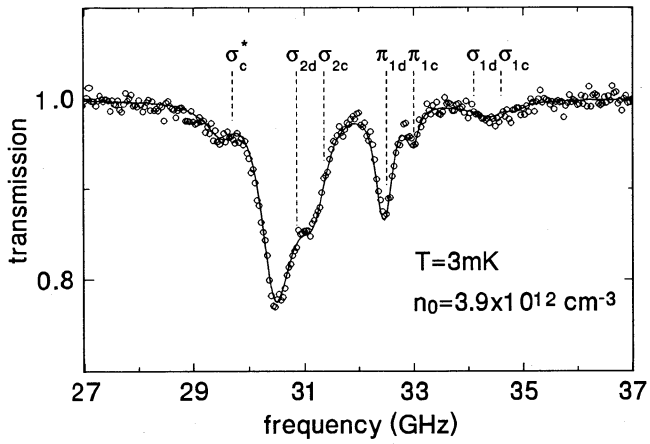

Fig. 6. Absorption spectrum, recorded with right-circularly polarized light. The *solid line* is a calculated spectrum for $T = 3 \pm 1$ mK and $n_0 = (3.9 \pm 1.7) \times 10^{12}$ cm^{-3}. The subscripts c and d refer to transitions from the corresponding ground states. The c state fraction $n_{c0}/n_0 \approx 0.1$. For the various lines the transition frequencies at $B = B_0$ are indicated

geometry used is characterized by $\alpha = 1.53$ T/cm, $\beta = 0.005$ T/cm^2, and $B_0 = 0.088$ T. The temperature of the trapped gas is so low that the ground state hyperfine structure starts to be resolved. We find for this spectrum $T = 3 \pm 1$ mK, $n_0 = (3.9 \pm 1.7) \times 10^{12}$ cm^{-3}, and a c state fraction $n_{c0}/n_0 \approx 0.1$. The line labeled σ_c^* corresponds to excitation to the $2^2P_{3/2}$, $m_j = -3/2$ state, which is weakly allowed due to the hyperfine mixing of the ground state. At this temperature the Doppler and Zeeman broadening are comparable to or smaller than the natural linewidth. The broadening of the lines is due to the fact that the density is so high that the sample is optically thick even for detunings much larger than the natural linewidth. The detected signal on resonance is not zero because the effective diameter of the sample is smaller than that of the incident L_α beam. Simultaneous determination of the temperature and density remains possible because the peak absorption is determined by the sample cross section (proportional to T), while the linewidth is largely determined by n_0.

9 Conclusion

We have introduced optical absorption spectroscopy as a diagnostic tool to study magnetically trapped H↑ at temperatures $T \lesssim 0.1$ K. By comparing experimental and theoretical spectra we are able to determine independently the temperature and the density. Our theoretical treatment allows us to describe the experimental spectra in detail, revealing several subtle polarization and dispersion effects.

Based on our current understanding we estimate that the method should be applicable down to sub-mK temperatures, for optically thick samples. The radial sample size at low temperatures can be matched to the L_α beam diameter by decreasing the radial field gradient α, thus maintaining a signal-to-noise ratio comparable to that at higher temperatures. This implies that spectroscopic diagnostics of the trapped gas should still be possible in the interesting regime of $T < 100$ μK and $n_0 > 10^{14}$ cm^{-3}, where quantum degeneracy is expected.

Acknowledgements. This research was supported by the Stichting voor Fundamenteel Onderzoek der Materie (FOM) and by the Nederlandse Organisatie voor Wetenschappelijk Onderzoek (NWO-PIONIER).

References

1. For reviews see I.F. Silvera, J.T.M. Walraven: In *Progress in Low Temperature Physics,* ed. by D.F. Brewer (North-Holland, Amsterdam 1986) Chap. **X**, p. 139
   I.F. Silvera, M.W. Reynolds: J. Low Temp. Phys. **87**, 343 (1992)
   J.T.M. Walraven: In *Fundamental Systems is Quantum Optics,* ed. by J. Dalibard, J.-M. Raimond, J. Zinn-Justin (Elsevier, Amsterdam 1992) pp. 487–544
2. A. Griffin (ed.): BEC-93 (Cambridge Univ. Press) (in press)
3. H.F. Hess: Phys. Rev. B **34**, 3476 (1986)
4. H.F. Hess, G.P. Kochanski, J.M. Doyle, N. Masuhara, D. Kleppner, T.J. Greytak: Phys. Rev. Lett. **59**, 672 (1987)
5. R. van Roijen, J.J. Berkhout, S. Jaakkola, J.T.M. Walraven: Phys. Rev. Lett. **61**, 931 (1988)
6. O.J. Luiten, H.G.C. Werij, I.D. Setija, M.W. Reynolds, T.W. Hijmans, J.T.M. Walraven: Phys. Rev. Lett. **70**, 544 (1993)
7. I.D. Setija, H.G.C. Werij, O.J. Luiten, M.W. Reynolds, T.W. Hijmans, J.T.M. Walraven: Phys. Rev. Lett. **70**, 2257 (1993)
8. O.J. Luiten: Lyman-α spectroscopy of magnetically trapped atomic hydrogen. Dissertation, University of Amsterdam (1993) (unpublished)
9. W. Wing: Prog. Quant. Electron. **8**, 181 (1984)
10. A. Lagendijk, I.F. Silvera, B.J. Verhaar: Phys. Rev. B **33**, 626 (1986)
    H.T.C. Stoof, J.M.V.A. Koelman, B.J. Verhaar: Phys. Rev. B **38**, 4688 (1988)
11. T.W. Hijmans, O.J. Luiten, I.D. Setija, J.T.M. Walraven: J. Opt. Soc. Am. B **6**, 2235 (1989)
12. S.J. Brodsky, R.J. Parsons: Phys. Rev. **163**, 134 (1967)
13. O.J. Luiten, H.G.C. Werij, I.D. Setija, M.W. Reynolds, T.W. Hijmans, J.T.M. Walraven: In *Proc. 13th Int'l Conf. on Atomic Physics,* ed. by H. Walther, T.W. Hänsch, B. Neizert (American Institute of Physics, New York 1993) p. 167
14. T. Bergeman, G. Erez, H.J. Metcalf: Phys. Rev. A **35**, 1535 (1987)
15. K. Helmerson, A. Martin, D.E. Pritchard: J. Opt. Soc. Am. B **9**, 483 (1992); B **9**, 1988 (1992)
16. R. Mahon, T.J. McIlrath, D.W. Koopman: Appl. Phys. Lett. **33**, 305 (1978)
17. H. Langer, H. Puel, H. Röhr: Opt. Commun. **34**, 137 (1980)
18. R. Hilbig, R. Wallenstein: IEEE J. QE-**15**, 1566 (1981)
19. G.C. Bjorklund: IEEE J. QE-**11**, 287 (1975)
20. L. Cabaret, C. Delsart, C. Blondel: Opt. Commun. **61**, 116 (1987)
21. J.P. Marangos, N. Shen, H. Ma, M.H.R. Hutchinson, J.P. Connerade: J. Opt. Soc. Am. B **7**, 1254 (1990)
22. K. Hakuta, L. Marmet, B.P. Stoicheff: Phys. Rev. A **45**, 5152 (1992)
23. Y.M. Yiu, T.J. McIlrath, R. Mahon: Phys. Rev. A **20**, 2470 (1979)
24. M. Krumrey, E. Tegeler, J. Barth, M. Krisch, F. Schäfers, R. Wolf: Appl. Opt. **27**, 4336 (1988)
25. P.P. Bey, H. Rabin: Phys. Rev. **162**, 794 (1967)
26. P.P. Bey, J.F. Giuliani, H. Rabin: Phys. Lett. **26A**, 128 (1968)
27. A.C. Michels, T. van Lieshout: Unpublished
28. D.C. Thompson, M.S. O'Sullivan, B.P. Stoicheff, G.-X. Xu: Cdn. J. Phys. **61**, 949 (1983)
29. W. Happer: Rev. Mod. Phys. **44**, 169 (1972)
30. H.A. Bethe, E.E. Salpeter: *Quantum Mechanics of One- and Two-Electron Atoms* (Plenum, New York 1977)